



Impact of longitudinal phase-matching variations on three-wave nonlinear interactions

CHRISTOPHE DORRER^{*}

Laboratory for Laser Energetics, University of Rochester, 250 East River Road, Rochester, NY 14623-1299,
USA

^{*}cdrerer@lle.rochester.edu

Abstract: A general study of three-wave nonlinear mixing in the presence of longitudinal variations in phase-matching conditions is presented. The efficiency of second-harmonic generation and optical parametric amplification is quantified using a normalized set of equations and a polynomial description of the wave-vector mismatch as a function of the longitudinal coordinate. These modeling results are used to estimate the impact of spatial variations in wave-vector mismatch experimentally obtained for five partially deuterated potassium dihydrogen phosphate crystals. The longitudinal inhomogeneities in the properties of crystals of similar quality are not expected to have a significant impact on their use for second-harmonic generation and optical parametric amplification, but the efficiency of nonlinear processes in crystals with larger variations could decrease.

© 2023 Optica Publishing Group under the terms of the [Optica Open Access Publishing Agreement](#)

1. Introduction

Nonlinear optics covers a very diverse range of interactions between optical waves [1]. Three-wave mixing corresponds to the interaction of waves at frequencies ω_1 , ω_2 , and $\omega_3 = \omega_1 + \omega_2$. It is widely used for nonlinear frequency conversion, e.g., resulting in an output wave at frequency 2ω generated from the input wave at frequency ω in second-harmonic generation (SHG), and parametric amplification resulting in energy transfer from the input pump at frequency ω_3 to the signal and idler at frequencies ω_1 and ω_2 . Efficient three-wave mixing requires phase matching. This requirement is generally expressed as $\Delta\mathbf{k} = \mathbf{k}_3 - \mathbf{k}_2 - \mathbf{k}_1 \approx \mathbf{0}$, where \mathbf{k}_j is the (vectorial) wave vector at frequency ω_j . For collinear interactions, this relation can be simply projected on the common propagation axis, but geometric angle-dependent terms introduced by noncollinear interactions lead to additional flexibility. In most cases, the resulting Δk does not depend on the transverse coordinates (in the plane perpendicular to the propagation direction) or longitudinal coordinate (along the propagation direction), based on the assumption that the local properties of the nonlinear medium are spatially uniform. In optical media where the propagation constant of the different waves can be controlled, a longitudinal variation in phase-matching properties can enhance the nonlinear conversion, e.g., increase its efficiency and bandwidth. Examples of these approaches include tapered optical fibers, aperiodic quasi-phase-matched structures, and nonlinear crystals with a temperature gradient [2–7].

While engineered changes in the longitudinal phase-matching properties can be advantageous, inherent uncontrolled variations are potentially detrimental to three-wave nonlinear mixing. For example, thermally induced changes in optical index and stoichiometric variations can have an impact on beam propagation and SHG efficiency [8–10]. Many nonlinear-optics applications are based on crystals with dimensions of the order of 1 cm, but much larger crystals are required for high-energy laser pulses. Frequency conversion of high-energy laser systems is based on large-aperture potassium dihydrogen phosphate (KDP) and its partially deuterated isomorph, DKDP: crystals with transverse dimensions of the order of 40 cm are used at the National Ignition Facility and the Laser Mégajoule [11–13]. DKDP can also support broadband optical parametric amplification (OPA) of a signal around 910 nm using a pump pulse generated by

frequency doubling of an Nd-doped laser. High-energy amplification stages rely on crystals with thickness and/or aperture larger than 5 cm, and much larger crystals would be required for the forecasted scaling to tens of petawatts [14–16]. Another application of large-scale KDP crystals is fourth-harmonic generation [17]. KDP and its isomorphs are currently the easiest crystals to grow at very large aperture, but the growth of lithium triborate (LBO) and cesium lithium borate (CLBO) has significantly progressed, leading to the availability of crystals with ~10-cm scale [18–21]. The spatial uniformity of large-aperture KDP/DKDP crystals, in particular local variations in crystalline axis orientation and deuteration level, has been investigated with a range of techniques. Spectrally resolved transmission and compositional analysis obtained, for example, by Raman spectroscopy are indicative of crystal homogeneity [22,23]. Micro-Raman spectroscopy, a technique that determines the deuteration level with sub-10- μm resolution in the transverse and longitudinal directions, has been used to understand the impact of deuteration on the observed retardance [24,25]. Optical techniques can provide quantitative estimates of the phase-matching properties, typically as a function of the transverse position within the aperture [26–28]. These studies have identified variations that could potentially impact local phase-matching conditions.

Various analyses of frequency conversion in bulk nonlinear crystals with linear [8,29,30] or sinusoidal [9] longitudinal variations in the wave-vector mismatch have been developed, and the impact of random duty-cycle errors has been analytically studied in quasi-phase-matched devices [31,32]. In this article, the impact of longitudinal variations in phase-matching conditions is quantified for second-harmonic generation and optical parametric amplification in bulk nonlinear crystals. The transverse wave-vector mismatch variations measured on five DKDP crystals are processed to estimate the effect on the efficiency of SHG and OPA in crystals with similar longitudinal variations. In Sec. 2, a system of normalized equations is presented to generally describe three-wave nonlinear mixing with longitudinal variations in wave-vector mismatch. Simulations of SHG and OPA quantify the impact of a wide range of wave-vector mismatches in Sec. 3. The spatial variations measured on five nonlinear crystals are assessed in Sec. 4.

2. Simulation framework

2.1. Longitudinal variations in phase-matching conditions

The nonlinear mixing of three waves at frequencies ω_1 , ω_2 , and $\omega_3 = \omega_1 + \omega_2$ in the plane-wave regime is considered. The spatial and temporal walk-off are assumed to be negligible for the sake of simplicity in this derivation, although including them in the simulations is straightforward. When the optical index n_j for the wave at frequency ω_j (at the correct polarization for phase matching of the nonlinear process) does not depend on the longitudinal position z , propagation from the input reference plane to the plane of coordinate z leads to an accumulated phase $k_j z$, where the propagation constant k_j is given by $k_j = n_j \omega_j / c$. A system of three nonlinear equations can then be derived in the slowly varying amplitude approximation to describe the propagation of the three fields E_j [1,33]. In the presence of longitudinal variations in optical index, a similar system of nonlinear equations can be derived (Appendix 1), provided that the relative longitudinal variations in optical index for each wave are small over distances of the order of their respective wavelength. This derivation shows that linear propagation, in the presence of longitudinal variations in k_j , leads to accumulation of a phase φ_j given by

$$\varphi_j(z) = \int_0^z k_j(z') dz'. \quad (1)$$

This phase (which simplifies to $k_j z$ in a medium with spatially uniform properties) leads to the phase mismatch $\Delta\varphi(z) = \varphi_3(z) - \varphi_1(z) - \varphi_2(z)$ at coordinate z . Taking this into account, the

propagation equations describing the nonlinear mixing of the three fields E_j are:

$$\frac{\partial E_1}{\partial z} = i \frac{\omega_1 d_{\text{eff}}}{cn_1} E_3 E_2^* \exp[i\Delta\varphi(z)], \quad (2a)$$

$$\frac{\partial E_2}{\partial z} = i \frac{\omega_2 d_{\text{eff}}}{cn_2} E_3 E_1^* \exp[i\Delta\varphi(z)], \quad (2b)$$

$$\frac{\partial E_3}{\partial z} = i \frac{\omega_3 d_{\text{eff}}}{cn_3} E_2 E_1 \exp[-i\Delta\varphi(z)], \quad (2c)$$

where d_{eff} is the effective nonlinearity and c is the speed of light.

When the crystal's properties are spatially varying, the local wave-vector mismatch can be decomposed as

$$\Delta k(x, y, z) = [\Delta k(x, y, z) - \langle \Delta k(x, y, z) \rangle] + \langle \Delta k(x, y, z) \rangle, \quad (3)$$

where $\langle \Delta k(x, y, z) \rangle$ is the average of Δk over the full crystal length L at a given transverse position (x, y) in the aperture. This term only depends on the transverse coordinates x and y , while the bracketed term in Eq. (3) corresponds to the longitudinal variation in wave-vector mismatch relative to its average value at these transverse coordinates. This article focuses on quantifying the impact of longitudinal variations in wave-vector mismatch. This is done for a nonlinear process that is either nominally phase matched [$\langle \Delta k(x, y, z) \rangle = 0$] or detuned from phase matching [$\langle \Delta k(x, y, z) \rangle \neq 0$].

2.2. Normalized equations

A system of normalized equations is derived from Eqs. (2) by defining normalized fields e_j such as

$$e_j = E_j \sqrt{\frac{\epsilon_0 c n_j}{2 \hbar \omega_j}} \kappa, \quad (4)$$

where κ is a constant. The form of Eq. (4) is chosen to introduce the field intensity, defined by

$$I_j = \frac{\epsilon_0 c n_j}{2} |E_j|^2, \quad (5)$$

and the photon energy $\hbar \omega_j$ at frequency ω_j . This makes the squared modulus of the normalized fields proportional to the number of photons at their respective frequency. A normalized longitudinal coordinate Z such as $z = LZ$ is used, where L is the length of the nonlinear medium and Z varies from 0 (input) to 1 (output). The phase mismatch relative to this variable is written as

$$\Delta\Phi(Z) = \Delta\varphi(LZ). \quad (6)$$

The variation in normalized wave-vector mismatch is

$$\Delta K(Z) = L \Delta k(LZ). \quad (7)$$

This relation allows for the scaling of the wave-vector variations Δk determined on one crystal to normalized wave-vector variations ΔK that can be used for integration of the system of normalized equations. The dephasing between the physical waves $\Delta\varphi$ and between the normalized waves $\Delta\Phi$ are identical after propagation from the input to the output. For example, a phase mismatch of 1 rad between input and output results from a constant normalized wave-vector mismatch $\Delta K = 1$, or equivalently, from a constant wave-vector mismatch $\Delta k = 1/L$.

The constant κ in Eq. (4) is identified by substitution of the three fields in one of the propagation equations, e.g., for Eq. (2a):

$$\frac{\partial e_1}{\partial Z} = i \frac{Ld_{\text{eff}}}{\kappa} \sqrt{\frac{2\hbar\omega_1\omega_2\omega_3}{n_1 n_2 n_3 c^3 \epsilon_0}} e_3 e_2^* \exp[i\Delta\varphi(z)]. \quad (8)$$

Choosing $\kappa = Ld_{\text{eff}} \sqrt{2\hbar\omega_1\omega_2\omega_3/n_1 n_2 n_3 c^3 \epsilon_0}$ leads to the following system of equations for e_j :

$$\frac{\partial e_1}{\partial Z} = ie_3 e_2^* \exp[i\Delta\Phi(Z)], \quad (9a)$$

$$\frac{\partial e_2}{\partial Z} = ie_3 e_1^* \exp[i\Delta\Phi(Z)], \quad (9b)$$

$$\frac{\partial e_3}{\partial Z} = ie_1 e_2 \exp[-i\Delta\Phi(Z)]. \quad (9c)$$

This normalized set of equations can be applied to the nonlinear mixing of three nondegenerate waves, for example, the evolution of the fields e_1 , e_2 , and e_3 of the signal, idler, and pump in an OPA, without consideration of their respective wavelength and the corresponding optical index. The same system of equations can be used for type-II SHG, with e_1 and e_2 representing the orthogonally polarized fields at the fundamental frequency ω_1 , and e_3 representing the field at the up-converted frequency $\omega_3 = 2\omega_1$. For type-I SHG, degeneracy of the two fields at the fundamental frequency leads to the following system of equations

$$\frac{\partial e_1}{\partial Z} = ie_3 e_1^* \exp[i\Delta\Phi(Z)], \quad (10a)$$

$$\frac{\partial e_3}{\partial Z} = \frac{i}{2} e_1^2 \exp[-i\Delta\Phi(Z)], \quad (10b)$$

where e_1 and e_3 represent the fields at the fundamental frequency (1ω) and up-converted frequency (2ω), respectively.

2.3. SHG and OPA in ideal phase-matching conditions

The system of Eqs. (10) has been integrated for phase-matched type-I SHG [$\Delta\Phi(Z) = 0$ at all Z] of a fundamental field at 1ω into a field at the up-converted frequency 2ω . The photon conversion efficiency expressed as the ratio of the output intensity at 2ω , $i_3(1)$ to the input intensity at 1ω , $i_1(0)$ is shown on Fig. 1(a). It increases toward its asymptotic limit, which corresponds to full up-conversion of the 1ω wave. Generation of one photon at 2ω requires two photons at 1ω , hence the asymptotic limit is equal to 0.5. The simulations that include the longitudinal variations of ΔK have been performed at $i_1(0) = 3$, which corresponds to a photon conversion efficiency of 0.35 [as indicated in Fig. 1(a)] and an intensity conversion efficiency of 70%.

The system of Eqs. (9) has been integrated as a function of the pump intensity for an OPA in ideal phase-matching conditions. The normalized input signal and idler intensities have been set at 10^{-3} and 0, respectively. The photon conversion efficiency, defined as the ratio of the output normalized signal intensity $i_1(1)$ to the input normalized pump intensity $i_3(0)$, has the typical exponential growth followed by a maximum and reconversion [Fig. 1(b)]. At $i_3(0) = 45.5$, each pump photon is converted into one signal photon and one idler photon, resulting in a saturated gain of 10^3 for the signal. The simulations that include the longitudinal variation of ΔK have been performed for a pump depletion equal to 100% [$i_3(0) = 45.5$] and 50% [$i_3(0) = 32.5$].

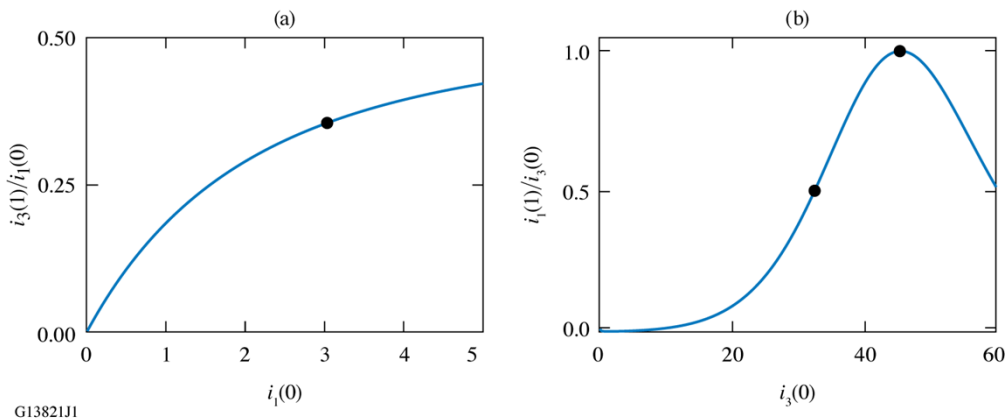


Fig. 1. (a) Photon conversion efficiency $i_3(1)/i_1(0)$ from 1ω to 2ω as a function of the normalized input 1ω intensity $i_1(0)$ for phase-matched type-I SHG. (b) Photon conversion efficiency $i_1(1)/i_3(0)$ from pump to signal as a function of the normalized input pump intensity $i_3(0)$ for a phase-matched OPA. The black circles indicate the operating regime for the simulations in the presence of longitudinal wave-vector variations

3. Simulations of three-wave nonlinear mixing in the presence of longitudinal variations in wave-vector mismatch

3.1. Representation of the longitudinal wave-vector mismatch

For simulations, the wave-vector mismatch ΔK was expressed as a sum of Legendre polynomials P_j having their argument between -1 and 1 and coefficients a_j that are randomly distributed in a specific range $[-\rho, \rho]$, following:

$$\Delta K(Z) = \sum_{j=1}^N a_j P_j(2Z - 1). \quad (11)$$

The largest considered coefficient range corresponds to $\rho = 1$ (note that a constant wave-vector mismatch with this value leads to a phase mismatch equal to 1 rad). A constant wave-vector mismatch (order = 0), a purely linear longitudinal variation (order = 1), and sum of polynomials with maximal orders equal to 1, 2, 3, and 5 have been considered to assess the sensitivity to the frequency of the longitudinal spatial variations (including orders larger than 5 did not lead to significantly different results beyond that). The sum is described by Eq. (11), which can represent the bracketed term in Eq. (3) because the integral of these Legendre polynomials is equal to 0. Non-phase-matched conditions correspond to the sum of Eq. (11) and a constant $\Delta\Phi_0$ that does not depend on Z . Integration of this constant between 0 and 1 leads to the phase mismatch $\Delta\Phi_0$ in the absence of longitudinal wave-vector mismatch variations.

3.2. Second-harmonic generation

The relative efficiency for an SHG process at $\Delta\Phi_0 = 0$ and $i_1(0) = 3$, resulting in an intensity conversion efficiency of 70%, is shown as a function of the range of Legendre coefficients ρ in Fig. 2(a) and as a function of the root mean square (rms) of the wave-vector mismatch σ in Fig. 2(b). The efficiency range (from lowest to highest efficiency) has been obtained by solving the system of three-wave nonlinear mixing equations for a large number of random polynomial descriptions of the longitudinal wave-vector mismatch. The observed range of conversion efficiency depends quadratically on ρ and σ , but its relative decrease is smaller than

1% over the considered range of Legendre coefficients. The SHG efficiency for a wave-vector mismatch ρ that is constant over the full crystal length, i.e., phase mismatch ρ after integration, is shown for reference. In that case, the efficiency decreases much faster than for sums of Legendre polynomials with similar coefficients and for polynomial wave vectors with similar standard deviation over the crystal length. A linear variation in wave vector has the smallest impact on the conversion efficiency (note that there is a one-to-one relation between the linear coefficient and the wave-vector rms value in this case, hence the curves describing the lowest and highest efficiency collapse into a single curve). Including a quadratic term leads to a larger range of efficiencies that extends toward lower values [Fig. 2(a)] and generally decreases the efficiency compared to a linear variation with the same standard deviation [Fig. 2(b)]. Polynomial terms beyond that do not have a significant impact on the conversion efficiency. This is attributed to the low-pass filtering effect of the integration process between wave vector ΔK and phase mismatch $\Delta\Phi$.

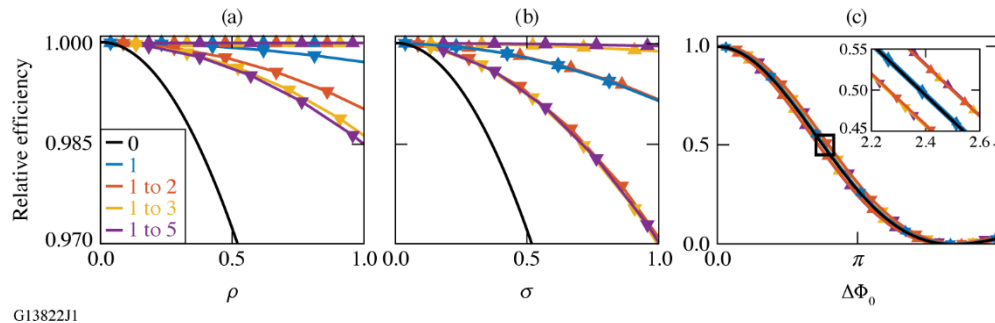


Fig. 2. [(a) and (b)] Relative efficiency of a nominally phase-matched SHG process with longitudinal variations in wave-vector mismatch. The mismatch is given by a sum of Legendre polynomials with a range of orders indicated in the legend and coefficients given by a random variable in the range $[-\rho, \rho]$, which is the horizontal axis in (a), whereas the horizontal axis in (b) is the rms of the wave-vector mismatch. (c) Relative efficiency of a phase-mismatched SHG process in the presence of longitudinal variations in phase matching given by a sum of Legendre polynomials with a range of orders indicated in the legend and coefficients given by a random variable in the range $[-0.5, 0.5]$. For all plots, the lines with markers indicate the lowest (triangles with apex pointing down) and highest (triangles with apex facing up) simulated efficiency.

The relative conversion efficiency of a phase-mismatched SHG process in the presence of longitudinal wave-vector variations is shown in Fig. 2(c) for the same input 1ω intensity. The horizontal axis corresponds to the constant phase mismatch $\Delta\Phi_0$ without longitudinal variations (in the fixed field approximation, the conversion efficiency is expected to fall to 0 at $\Delta\Phi_0 = 2\pi$, but operation in the high-conversion-efficiency regime modifies this condition). The wave-vector mismatch is represented by a sum of Legendre polynomials with random coefficients uniformly distributed in the range $[-0.5, 0.5]$. The impact of these longitudinal variations is noticeably larger than in the case of phase-matched SHG, with the exception that a linear variation in wave-vector mismatch has no significant impact on the SHG efficiency [inset of Fig. 2(c)]. For higher-order variations, the SHG efficiency ranges for example from 0.46 to 0.535, whereas it ranged from 0.996 to 1 in the phase-matched configuration. The degradation in conversion efficiency is dominated by the quadratic variations, and the larger polynomial orders do not significantly modify the efficiency. Simulations of the phase-mismatched SHG process for different values of ρ indicate that the resulting range of SHG efficiency approximately scales like ρ , instead of ρ^2 in the phase-matched case. This observation is consistent with the analysis of SHG in the low-conversion-efficiency regime presented in Appendix 2.

3.3. Optical parametric amplification

The procedure described in the previous section has been applied to a phase-matched OPA. The signal intensity has been set to 10^{-3} and no idler is present at the input. Figures 3 and 4 present the efficiency of an OPA with 100% depletion [$i_3(0) = 45.5$] and 50% depletion [$i_3(0) = 32.5$], respectively. The efficiency generally decreases quadratically with the range of the longitudinal variations ρ [Figs. 3(a) and 4(a)] and the rms [Figs. 3(b) and 4(b)] of the wave-vector mismatch. The impact of the longitudinal variations in phase-matching conditions is small, and does not depend significantly on the presence of higher-order variations in the longitudinal wave-vector mismatch ΔK . The minimal efficiency for a given ρ is of the order of the efficiency observed for a constant $\Delta K = \rho$. For an OPA operated in full pump depletion, the polynomial variations in ΔK can lead to a lower output signal intensity than a constant ΔK with similar value [Figs. 3(a) and

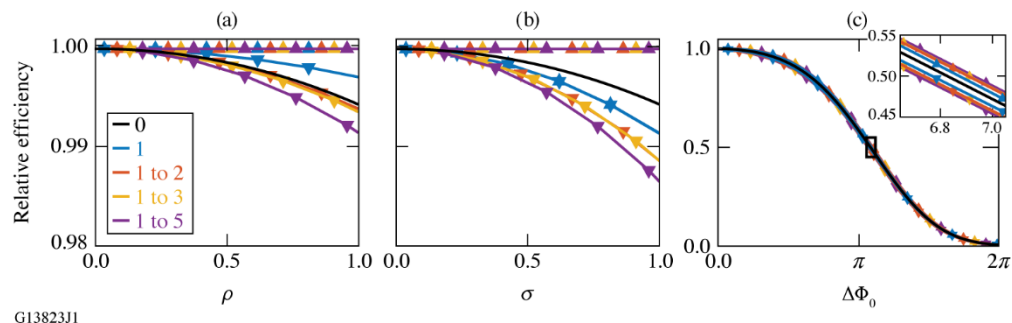


Fig. 3. Relative efficiency of an OPA operating at 100% pump depletion. The mismatch is given by a sum of Legendre polynomials with a range of orders indicated in the legend and coefficients given by a random variable in the range $[-\rho, \rho]$, which is the horizontal axis in (a), whereas the horizontal axis in (b) is the rms of the wave-vector mismatch. (c) Relative efficiency of a phase-mismatched OPA in the presence of longitudinal variations in phase matching given by a sum of Legendre polynomials with a range of orders indicated in the legend and coefficients given by a random variable in the range $[-0.5, 0.5]$. For all plots, the lines with markers indicate the lowest and highest simulated efficiency.

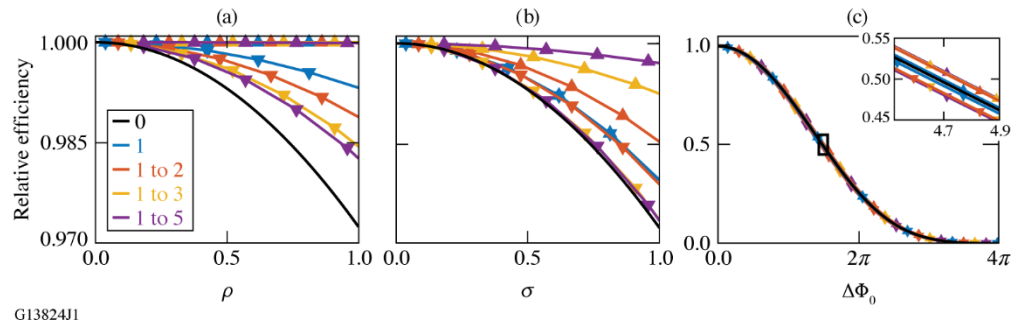


Fig. 4. Relative efficiency of an OPA operating at 50% pump depletion. The mismatch is given by a sum of Legendre polynomials with a range of orders indicated in the legend and coefficients given by a random variable in the range $[-\rho, \rho]$, which is the horizontal axis in (a), whereas the horizontal axis in (b) is the rms of the wave vector. (c) Relative efficiency of a phase-mismatched OPA in the presence of longitudinal variations in phase matching given by a sum of Legendre polynomials with a range of orders given in the legend and coefficients given by a random variable in the range $[-0.5, 0.5]$. For all plots, the lines with markers indicate the lowest and highest simulated efficiency.

3(b)]. This is different from SHG, for which a constant ΔK yields the lowest efficiency. The impact on OPA efficiency is larger when the pump intensity is lowered to yield half the maximal output signal intensity, and in that case, a constant ΔK yields a lower efficiency than polynomial variations [Figs. 4(a) and 4(b)].

Operating the OPA around the average phase mismatch $\Delta\Phi_0$ leads to a decrease in amplified signal intensity. When the longitudinal wave-vector mismatch is modeled by a sum of Legendre polynomials with random coefficients in the range $[-0.5, 0.5]$, the impact on the output signal intensity is smaller than for SHG [Figs. 3(c) and 4(c)]. The range of observed efficiencies for a given $\Delta\Phi_0$ increases and saturates when higher polynomial orders are included. As was the case for SHG, the range of efficiencies observed for a detuned OPA scales like the range of longitudinal polynomial variations ρ .

4. Application to five DKDP crystals

4.1. General data analysis

In the absence of a nondestructive technique to directly determine the longitudinal variations of the phase-matching conditions in nonlinear crystals, experimental data corresponding to transverse variations in phase-matching conditions determined via detuned SHG has been used [26]. In that technique, the transverse variations in wave-vector mismatch are calculated using the relation between SHG energy and wave-vector mismatch determined in the fixed-field approximation for a plane wave. The measured SHG energy $E_{\text{SHG}}(x,y)$ is normalized into a relative energy variation $S(x,y) = E_{\text{SHG}}(x,y)/\langle E_{\text{SHG}} \rangle - 1$, where $\langle E_{\text{SHG}} \rangle$ is the average energy across the aperture. The wave-vector variation is then calculated using $\Delta k_{\text{SHG}} = S(x,y)/L\zeta$, where L is the crystal thickness and ζ is a constant. For small variations in wave-vector mismatch, the obtained $\Delta k_{\text{SHG}}(x,y)$ is assumed to be $\langle \Delta k_{\text{SHG}}(x,y,z) \rangle$, the average of the wave-vector mismatch along the longitudinal variable z as a function of the transverse variables x and y . This assumption is supported by the observation that, for the variations in Δk that are consistent with measured data, the SHG energy averages out to its value calculated from the average wave-vector mismatch [Fig. 2(c)].

Under the assumption of anisotropy of the spatial variations in phase-matching conditions, lineouts of the measured $\Delta k_{\text{SHG}}(x,y)$, where x and y are transverse coordinates, are used to estimate the variations in Δk_{SHG} as a function of the longitudinal coordinate z . For example, $\Delta k_{\text{SHG}}(x,0)$, where x varies from $-L/2$ to $L/2$, is taken as an example of possible variations in $\Delta k_{\text{SHG}}(z)$, where z varies from 0 to L . A given 2-D map of transverse variations in Δk can therefore yield several samples of longitudinal variations. This approach is not generally supported by specific knowledge on crystal growth nor empirically confirmed in the absence of a direct spatially resolved (in three dimensions) determination of phase-matching conditions, i.e., there is no mathematical or physical reason why the determined samples are representative of actual longitudinal variations in the crystal under test. In practice, the inhomogeneity in the crystal's properties is most likely correlated to changes in the growth solution and environmental conditions during the growth process, as well as location within the boule. In most cases (and certainly for type-I SHG and OPA, which are the main cases of interest in this article), phase matching requires that the waves propagate at a specific angle relative to the crystal axis, i.e., there is a definite angle of the crystalline planes relative to the propagation axis. Although the actual longitudinal variations in phase-matching conditions are most likely different from what is determined under these assumptions (in overall magnitude and spatial scale), the determined order of magnitude is essential to judge their potential impact in practical applications. The measured phase mismatch depends on the bulk variations within the crystal and changes in propagation angle caused by refraction at the input surface [26]. The latter, which are caused by coating imperfections, are restricted to high frequencies, which do not have a significant impact (Sec. 3). Hence, the determined wave-vector mismatch has not been post-processed to isolate the bulk variations.

A subset of the wave-vector mismatch determined on five DKDP crystals has been used. These crystals were designed for studies of broadband optical parametric chirped-pulse amplification (OPCPA) around 910 nm by a pump pulse at 526.5 nm. Their main characteristics are listed in Table 1. The listed deuteration level corresponds to a vendor specification. A deuteration level that is consistent with specific sets of Sellmeier equations has been previously determined using a two-wavelength phase-matching technique [34]. It was found to be within a few percent of the deuteration level determined by the vendor using pycnometric measurements of the solution during growth. The small-aperture crystals (25-mm transverse dimensions) have been used for scientific studies while the large-aperture crystals (63-mm transverse dimension) support high-energy broadband parametric amplification in an OPCPA system [16]. For reference, the measured variations in $\Delta k_{\text{SHG}}(x,y)$ for each crystal in one specific orientation relative to the input beam are shown in Appendix 3. The magnitude of this quantity is of the order of 5 m^{-1} . In the fixed field approximation, the SHG energy generated in a crystal of length L is proportional to $[\sin(\Delta k_{\text{SHG}}L/2)/(\Delta k_{\text{SHG}}L/2)]^2$. With the observed wave-vector mismatch, the SHG energy would therefore decrease by 0.5% because of transverse variations in wave-vector mismatch in crystals with $L = 50$ mm. The decrease is insignificant when considering thicknesses that are commonly used for SHG of nanosecond lasers, e.g., $L = 12$ mm. The wave-vector mismatch variations are consistent with angular variations of the order of $10 \mu\text{rad}$ and deuteration variation of the order of 0.01% in the five crystals.

Table 1. Characteristics of the five DKDP crystals used in this study.

TableCrystal	Nominal deuteration level	Longitudinal dimension	Transverse dimension (physical/characterized)
1	70	48	63/48
2	70	52	63/48
3	80	48	25/22
4	92	48	25/22
5	98	48	25/22

General information relating to variations in wave-vector mismatch for these crystals is presented in Fig. 5. First, the absolute value of the difference between $\Delta k_{\text{SHG}}(x, y)$ and its value at the center of the aperture $\Delta k_{\text{SHG}}(0,0)$ is calculated for all points in the aperture, binned as a function of the distance to the center, and averaged for each bin. The resulting plot indicates the average increase in measured wave-vector mismatch as a function of the transverse distance. Several measurements were performed on each crystal, e.g., after 180° rotations, resulting in slightly different but generally consistent determinations. For a given crystal, the wave-vector mismatch increases approximately linearly with the distance [Fig. 5(a)] and the corresponding slopes show the variations for the different crystals [Fig. 5(b)]. Crystal 1 has distinctly smaller variations than crystal 2, the latter having similar variations to crystals 3 and 4. The largest variations are observed on crystal 5, which has the highest deuteration level. A mild dependence of the variation amplitude with deuteration level, with higher deuteration levels yielding larger variations, is observed. However, these data alone should not lead to a general conclusion on the impact of deuteration level because it is limited to a few samples, with crystal 5 being a clear outlier. The typical dependence of the wave-vector mismatch with distance is of the order of $0.1 \text{ m}^{-1}/\text{mm}$ for crystals 2, 3 and 4, e.g., the wave-vector mismatches for two points separated by 10 mm differ on average by 1 m^{-1} . Crystal 1 has lower variations, whereas crystal 5 has higher variations. The standard deviation of the wave-vector mismatch over the characterized aperture has been calculated for the five crystals [Fig. 5(c)]. Based on the approximately linear increase in Δk_{SHG} with distance, the standard deviation is scaled to a 10-mm aperture, i.e., divided by the linear transverse scale of the data set for each crystal (48 mm for the large-aperture crystals and

22 mm for the small-aperture crystals) and multiplied by 10 mm. The resulting scaled standard deviation σ shows similar variations for crystals 2 to 4 ($\sim 0.5 \text{ m}^{-1}$ over a 10-mm aperture), with lower variations for crystal 1 and significantly higher variations for crystal 5 ($\sim 1.5 \text{ m}^{-1}$ over a 10-mm aperture).

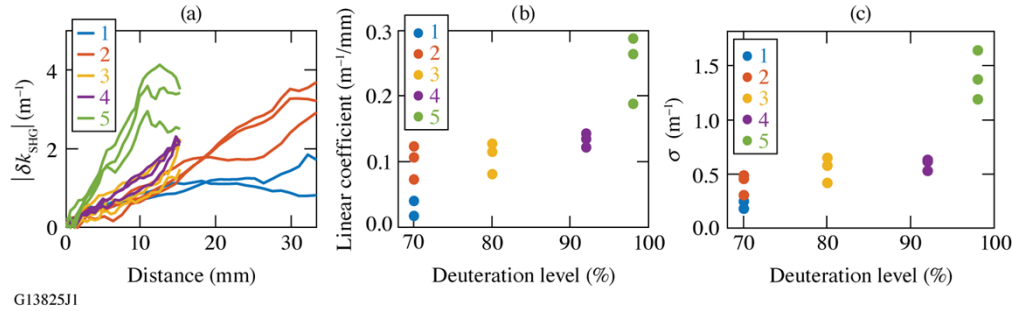


Fig. 5. (a) Average magnitude of the wave-vector mismatch difference at all transverse points in the aperture relative to its value at the center for crystals 1 to 5. (b) Linear fit coefficient of the data shown in (a). (c) Standard deviation σ of the wave-vector mismatch across the aperture of crystal 1 to 5 after normalization to a 10-mm aperture.

For integration over the normalized range [0,1] and consistency with the simulations presented in Sec. 3, the normalized longitudinal wave-vector mismatch ΔK is calculated from the measured Δk lineout restricted to the integration length after multiplication by this length [Eq. (7)]. The chosen integration length depends on the nonlinear process, as discussed below for SHG and OPA. Fitting of each of the obtained wave-vector mismatches ΔK by a sum of Legendre polynomial yields

$$\Delta K(Z) \approx \sum_{j=1}^N b_j P_j(2Z - 1), \quad (12)$$

where b_j is the respective coefficient of the Legendre polynomial P_j . These coefficients are then used as an experimental benchmark for comparison to the simulations presented in Sec. 3.

4.2. Second-harmonic generation at 1053 nm

For SHG of nanosecond pulses, a length $L_{\text{SHG}} = 12 \text{ mm}$ is chosen based on the typical thickness of doublers used on laser facilities generating high-energy nanosecond pulses [12]. Lineouts representative of the variations in Δk over that length are extracted from the experimental data shown in Appendix 3. For the three small-aperture crystals, four representative lineouts that contain the center of the aperture and extend either horizontally or vertically from that point toward $x > 0$, $x < 0$, $y > 0$, or $y < 0$ are chosen. For the two large-aperture crystals, a total of eight lineouts are chosen along a vertical or horizontal line that goes through the center of the aperture. For SHG of a source at 1053 nm, the wave-vector mismatch has the same expression as the experimentally determined wave-vector mismatch, and the latter can directly be used (Sec. 4.4 discusses SHG at other wavelengths). The corresponding Legendre coefficients $\{b_j\}$ for the resulting 20 sets of ΔK are shown in Fig. 6. For these crystals, the magnitude of the coefficients b_j is smaller than 0.1 over all orders. It is smaller than 0.015 for orders higher than 5, and only reaches values higher than that for lower orders. Considering the simulation results for SHG (Fig. 2), these longitudinal variations have no significant impact on the SHG process for a crystal that is either nominally phase matched or detuned from phase matching. Additionally, the wave-vector standard deviation over a 10-mm distance is of the order of 1 m^{-1} for these crystals [Fig. 5(c)]. This corresponds to σ of the order of 0.01 for the normalized ΔK , which

has negligible impact on SHG [Fig. 2(b)]. Longitudinal variations in wave-vector mismatch are therefore not expected to have any significant impact on SHG in crystals of this quality.

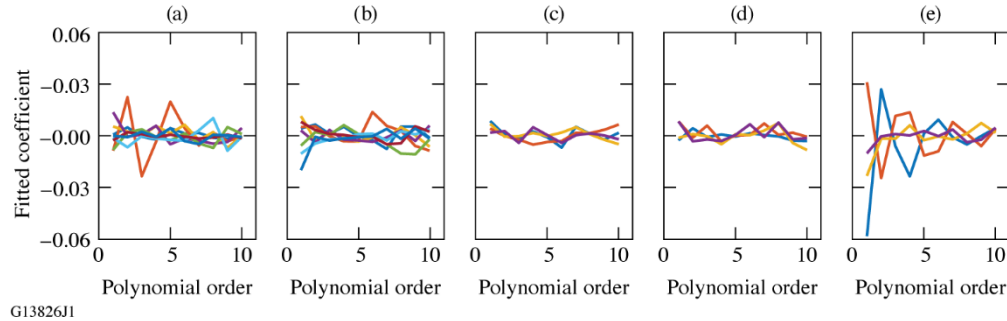


Fig. 6. Legendre coefficients for SHG in a 12-mm-thick crystal derived from data obtained on crystals 1 to 5 [from (a) to (e), respectively].

4.3. Spectrally degenerate OPA pumped at 526.5 nm

For OPA analysis, a thickness $L_{\text{OPA}} = 48$ mm is chosen. This is similar to the length of the DKDP crystals that have been used on MTW-OPAL [16] and is essentially the largest transverse dimension over which wave-vector mismatch data has been obtained (although one could consider lineouts along the two diagonals of each large-aperture crystal). Only data from the large-aperture crystals are used, resulting in four lineouts (a horizontal lineout and a vertical lineout for each of the two crystals) over the distance L_{OPA} . The wave-vector mismatch experimentally determined using SHG at 1053 nm can only be applied directly to a spectrally degenerate OPA with a pump at 526.5 nm, which has the same wave-vector mismatch expression relative to variations in deuteration and crystal angle. In that case, a total of four lineouts corresponding to the measured δk on the two large-aperture crystals are used, with a length of 48 mm and vertical or horizontal orientation. The resulting lineouts [obtained using Eq. (7)] are then fitted by Legendre polynomials [Figs. 7(a) and 7(b)]. These coefficients are different from those corresponding to Figs. 6(a) and 6(b) because (1) they span the full aperture of the crystals, and (2) they are scaled differently for integration over the longer crystals. Comparison of these coefficients with the range of coefficients covered by the simulations (Figs. 3 and 4) indicates that the OPA efficiency is not expected to be significantly impacted. This conclusion is extended to even longer crystals

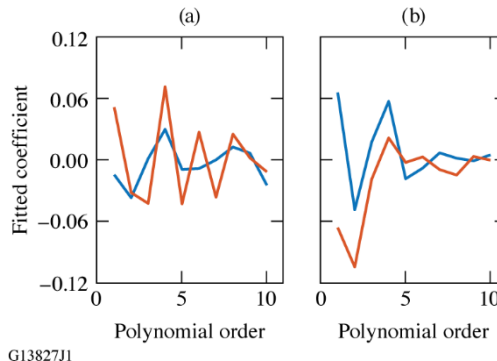


Fig. 7. Legendre coefficients for a spectrally degenerate OPA in a 48-mm-thick crystal derived from data obtained on crystal 1 and 2 [(a) and (b), respectively].

such as the one used on the PEARL laser ($L_{\text{OPA}} = 80$ mm) [14]. Considering that the variations in δk for a given crystal scale on average like the distance, an increase by a factor of 2 in L_{OPA} does not lead to a significant degradation in OPA efficiency, provided that the crystal quality is similar to those tested in this study. This conclusion is also valid for crystal 5, which has wave-vector mismatch variations a few times worse than the other crystals.

4.4. Wave-vector mismatch at other wavelengths

The relevance of the wave-vector mismatch variations experimentally determined using SHG at 1053 nm to SHG at other wavelengths is estimated by considering the impact of variations in internal angle $\delta\theta$ and deuteration level δX . For a crystal that has been tuned to achieve phase matching for SHG at the wavelength λ_1 (resulting in a wave at the wavelength $\lambda_3 = \lambda_1/2$), the local variations in wave-vector mismatch Δk_{SHG} are

$$\begin{aligned} \Delta k_{\text{SHG}}(\lambda_1) &= \frac{4\pi}{\lambda_1} [n_e(\lambda_3, \theta + \delta\theta, X + \delta X) - n_o(\lambda_1, X + \delta X)] \\ &= \frac{4\pi}{\lambda_1} [\partial_{\theta,3} n_e \delta\theta + (\partial_{X,3} n_e - \partial_{X,1} n_o) \delta X] \\ &= \partial_\theta \Delta k_{\text{SHG}} \delta\theta + \partial_X \Delta k_{\text{SHG}} \delta X, \end{aligned} \quad (13)$$

where the variations in the local angle of the crystal axis relative to the propagation axis $\delta\theta$ and the local deuteration level δX depend on the longitudinal position. In Eq. (13), $\partial_{\theta,3} n_e$ is the partial derivative (with respect to the angle θ) of the extraordinary index at the wavelength λ_3 , and $\partial_{X,j} n$ is the partial derivative (with respect to the deuteration level X) of the index n (either ordinary or extraordinary) at the wavelength λ_j . For the range of wavelengths over which the partial derivatives in Eq. (13) do not change significantly, the local variations in crystal properties (angle and deuteration level) therefore yield similar variations around phase matching after scaling by the ratio of the wavelength at which the characterization was performed (1053 nm) and the wavelength at which SHG is performed (λ_1). The partial derivatives in Eq. (13) vary approximately by 10% over a 100-nm interval around 1053 nm [Figs. 8(a) and 8(b)]. This indicates that such characterization would lead to an acceptable estimate of SHG performance at other wavelengths within that range.

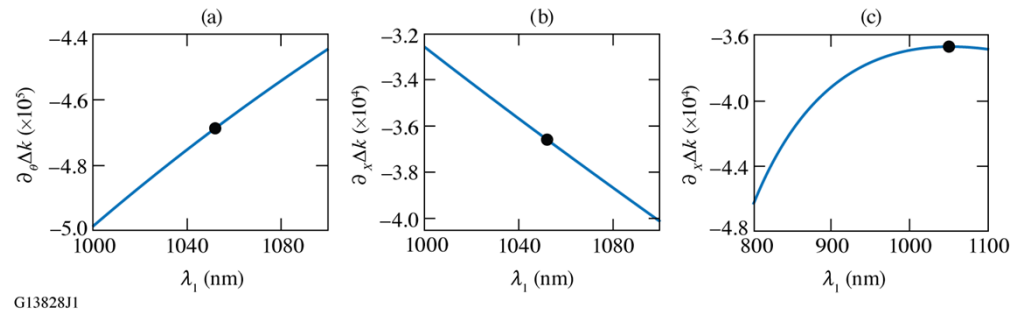


Fig. 8. Derivative of the wave-vector mismatch in 70% DKDP for SHG at wavelength λ_1 with respect to (a) phase-matching angle, (b) deuteration level, and (c) derivative of the wave-vector mismatch for an OPA pumped at $\lambda_3 = 526.5$ nm and a signal at wavelength λ_1 with respect to deuteration level. The black circles indicate the wavelength at which the crystal's characterization based on SHG has been done.

Another case of interest is the operation of a spectrally nondegenerate OPA, with a signal, idler, and pump at wavelengths λ_1 , λ_2 , and λ_3 , for which the local variation in wave-vector mismatch Δk_{OPA} can be written as

$$\begin{aligned} \Delta k_{\text{OPA}}(\lambda_1) &= \frac{2\pi}{\lambda_3} n_e(\lambda_3, \theta + \delta\theta, X + \delta X) - \frac{2\pi}{\lambda_1} n_o(\lambda_1, X + \delta X) - \frac{2\pi}{\lambda_2} n_o(\lambda_2, X + \delta X) \\ &= \frac{2\pi}{\lambda_3} \partial_{\theta,3} n_e \delta\theta + \left[\frac{2\pi}{\lambda_3} \partial_{X,3} n_e - \frac{2\pi}{\lambda_1} \partial_{X,1} n_o - \frac{2\pi}{\lambda_2} \partial_{X,2} n_o \right] \delta X \quad (14) \\ &= \partial_\theta \Delta k_{\text{OPA}} \delta\theta + \partial_X \Delta k_{\text{OPA}} \delta X. \end{aligned}$$

The angular partial derivatives in Eqs. (13) and (14) have a similar value when the OPA pump wavelength is equal to the wavelength of the frequency-converted wave in the SHG case (assuming that the phase-matching angles for these two processes are similar). This implies that local variations in angles have a similar impact on these two processes. The local variations in deuteration level have an impact that depends on the signal wavelength [Fig. 8(c)]. The corresponding partial derivative changes by approximately 20% between 800 and 1053 nm. Therefore, SHG characterization can also provide a good estimate of wave-vector variations in the case of a broadband OPA operating over this range, although the accuracy decreases when the signal wavelength is further away from spectral degeneracy.

5. Conclusions

This general study quantifies the effect of longitudinal variations in wave-vector mismatch on second-harmonic generation and optical parametric amplification. Low-order variations have been shown to have the largest impact on efficiency. These variations decrease the efficiency of nonlinear processes that are nominally phase matched. A larger range of efficiencies around the average efficiency is observed for processes that are not nominally phase matched. No single metric has been identified to quantify the efficiency impact of low-order variations in phase-matching conditions, unlike in quasi-phase-matched structures in which the efficiency decrease can be analytically linked to the statistical properties of random duty-cycle errors [31,32].

The transverse variations in wave-vector mismatch measured on five commercial DKDP crystals provide estimates of the longitudinal variations that can be expected on these crystals. Comparison of these estimates with modeling results indicates no significant impact of the longitudinal wave-vector variations on three-wave nonlinear mixing. However, the much larger variations in angular axis orientation and deuterium content that have been documented on some crystals [22,23,27] could, if present in the longitudinal direction, have an impact on efficiency because of its quadratic dependence with respect to variations. The process described in this article could be applied to other crystals, and in particular to larger DKDP crystals that are required to support multipetawatt laser facilities. Scaling to higher energies requires an increase in transverse aperture for these crystals, but their longitudinal dimension is not expected to change significantly because of efficiency and spectral acceptance considerations. Transverse variations are therefore expected to have a larger impact than longitudinal variations for the crystals supporting high-peak-power facilities, provided that their quality is comparable to that of the smaller crystals considered in this study. The development of metrology techniques to quantify the spatial variations in nonlinear crystals' properties and their impact on wave mixing remains an important challenge for the development of large-scale lasers.

Appendix 1

This appendix presents a derivation of the system of propagation equations for three-wave nonlinear mixing in the presence of longitudinal variations in propagation constants and the underlying assumptions. Combining the notations and derivations from Refs. [1] and [33], the field at frequency ω_j obeys the equation

$$\Delta \mathbf{E}_j(\mathbf{r}) + \frac{\omega_j^2}{c^2} \boldsymbol{\varepsilon}^{(1)}(\omega_j) \cdot \mathbf{E}_j(\mathbf{r}) = -\frac{\omega_j^2}{\varepsilon_0 c^2} \mathbf{P}_j^{\text{NL}}(\mathbf{r}), \quad (15)$$

where \mathbf{E}_j is the vectorial field, $\boldsymbol{\varepsilon}_j$ is the dielectric tensor, \mathbf{P}_j^{NL} is the nonlinear polarization source term, and \mathbf{r} is the position (dependent on the two transverse coordinates and one longitudinal coordinate). In the remainder of this appendix, the transverse variations of the fields and their losses are neglected.

Equation (15) can first be solved in the absence of the nonlinear source term. It is postulated that the field E_j can be expressed as

$$E_j(z, t) = \text{Re}(E_j \exp\{i[\varphi_j(z) - \omega_j t]\}), \quad (16)$$

where E_j is a constant amplitude and φ_j is a phase to be determined. Substitution of Eq. (16) into Eq. (15) leads to

$$-\left(\frac{\partial \varphi_j}{\partial z}\right)^2 + i \frac{\partial^2 \varphi_j}{\partial z^2} + \frac{\omega_j^2 n_j^2(z)}{c^2} = 0, \quad (17)$$

where $\varepsilon_j(z) = n_j^2(z)$ by definition. With the assumption $|\partial^2 \varphi_j / \partial z^2| \ll (\partial \varphi_j / \partial z)^2$ (to be checked later), the resolution of Eq. (17) yields

$$\varphi_j(z) = \int_0^z \frac{n_j(z') \omega_j}{c} dz' = \int_0^z k_j(z') dz', \quad (18)$$

i.e., linear propagation of each wave simply adds a phase given by the integral of its propagation constant k_j . The assumption stated above corresponds to

$$\frac{1}{n_j} \frac{\partial n_j}{\partial z} \ll k_j, \quad (19)$$

i.e., the relative longitudinal variations in optical index for each wave are small over distances of the order of their respective wavelength.

When nonlinear mixing occurs during propagation, the field is assumed to be given by Eq. (16), in which the amplitude is now a slowly varying function of the longitudinal coordinate z . After substitution of Eq. (16) with the solution given by Eq. (18), the left-hand side of Eq. (15) applied to $j=1$ can be developed and simplified into

$$\frac{\partial^2 E_1}{\partial z^2} + 2i \frac{\partial E_1}{\partial z} k_1 + i E_1 \frac{\partial^2 \varphi_1}{\partial z^2} - E_1 k_1^2 + E_1 \frac{\omega_1^2}{c^2} \varepsilon_1 = 2i \frac{\partial E_1}{\partial z} k_1, \quad (20)$$

in the slowly varying approximation for the field amplitude ($|\partial^2 E_1 / \partial z^2| \ll k_1 |\partial E_1 / \partial z|$). The propagation term for E_1 must equate the nonlinear source term, which is proportional to the fields E_2^* and E_3 . This leads to

$$\frac{\partial E_1}{\partial z} = i \frac{\omega_1 d_{\text{eff}}}{cn_1(z)} E_3 E_2^* \exp[i\Delta\varphi(z)], \quad (21)$$

where $\Delta\varphi(z) = \varphi_3(z) - \varphi_1(z) - \varphi_2(z)$. One should note that the spatially varying n_1 appears in Eq. (21). Under the assumption (supported by the experimental investigations referenced in

this article) that the variations in optical index in good-quality crystals are relatively small, the local optical index can be replaced by a constant value, e.g., its average value over the crystal's volume, in Eq. (21) and its equivalent formulations for the propagation of E_2 and E_3 . Equations functionally equivalent to Eq. (21) have been used for example in Refs. [2,5,6,7] and [9] to describe the propagation of fields in media with longitudinally varying propagation constants.

Appendix 2

For SHG in the low-conversion regime, one can assume that the fundamental field e_1 is undepleted. The field at the output ($Z = 1$) can be obtained by direct integration of Eq. (10)(b) between 0 and 1, leading to

$$e_3(1) = \frac{1}{2}e_1^2 \int_0^1 \exp[-i\Delta\Phi(Z)] dZ = \frac{1}{2}e_1^2 \int_0^1 \exp\left[-i \int_0^Z \Delta K(Z') dZ'\right] dZ. \quad (22)$$

Using the equivalent of Eq. (3) for ΔK , Eq. (22) can be written as

$$e_3(1) = \frac{1}{2}e_1^2 \int_0^1 \exp\left(-i \int_0^Z \langle \Delta K \rangle dZ'\right) \exp\left\{-i \int_0^Z [\Delta K(Z') - \langle \Delta K \rangle] dZ'\right\} dZ, \quad (23)$$

where $\langle \Delta K \rangle$ is the longitudinal average of ΔK . The first exponential term in Eq. (23) is simply

$$\exp\left(-i \int_0^Z \langle \Delta K \rangle dZ'\right) = \exp(-i \langle \Delta K \rangle Z). \quad (24)$$

Assuming that the variations in ΔK around its average are relatively small, one can develop the second exponential term in Eq. (23) as

$$\exp\left\{-i \int_0^Z [\Delta K(Z') - \langle \Delta K \rangle] dZ'\right\} = 1 - i \int_0^Z [\Delta K(Z') - \langle \Delta K \rangle] dZ'. \quad (25)$$

In nominally non-phase-matched conditions ($\langle \Delta K \rangle \neq 0$), the zeroth- and first-order terms in Eq. (25) are generally sufficient to approximate the intensity at 2ω , which is proportional to

$$|e_3(1)|^2 \propto \left| \int_0^1 \exp(-i \langle \Delta K \rangle Z) dZ \right|^2 + 2 \text{Im} \left\{ \int_0^1 \exp(i \langle \Delta K \rangle Z) dZ \int_0^1 \exp(-i \langle \Delta K \rangle Z) \int_0^Z [\Delta K(Z') - \langle \Delta K \rangle] dZ' dZ \right\}, \quad (26)$$

provided that its second term on the right-hand side (which is proportional to the variations in ΔK around its average) is the leading term in the development. Numerical investigation shows that this is not the case for variations given by the Legendre polynomial of first order, implying that these do not have a significant impact for phase-mismatched SHG. That term, however, is nonzero for variations given by the Legendre polynomial of second order. In these conditions, the induced range of efficiencies is symmetric relative to the efficiency for a constant phase mismatch [the first term in Eq. (26)] since a change of sign in variations relative to the average leads to a

change of sign in the induced efficiency variation. It scales linearly with the variations in ΔK , e.g., like the range of polynomial coefficients ρ used to describe the variations of ΔK around its average value.

In nominally phase-matched conditions ($\langle \Delta K \rangle = 0$), the second term in Eq. (26) is equal to 0, implying that higher-order terms must be included in the approximation of the 2ω intensity. These terms scale like the square of the variations in ΔK around its average (equal to 0). The induced decrease in efficiency scales like the square of the range of polynomial coefficients ρ used to describe ΔK .

These derivations, which have been obtained for small SHG conversion efficiencies, are consistent with what was observed for the SHG conversion efficiencies presented in Sec. 3.1, which have been performed in the high-conversion-efficiency regime.

Appendix 3

The transverse variations in Δk for SHG at 1053 nm determined via spatially resolving the SHG energy produced by the crystal under test detuned from phase matching [26] are shown in Fig. 9 for the five DKDP crystals used in this study.

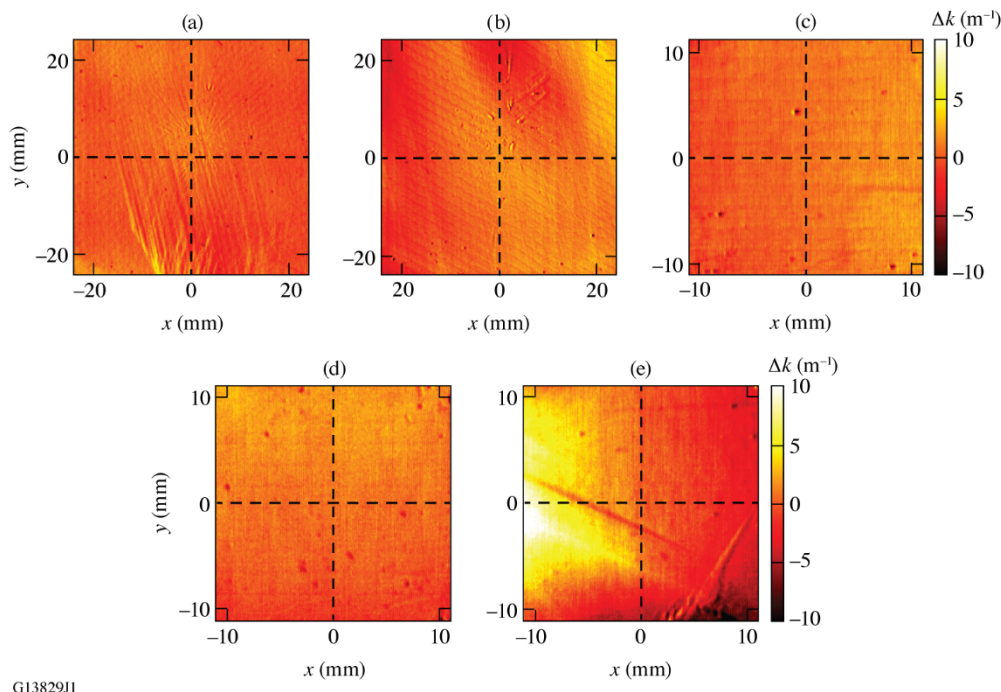


Fig. 9. Maps of transverse variations in Δk for crystals 1 to 5 [from (a) to (e), respectively]. The dashed lines indicate the location of the lineouts used for calculations of the Legendre coefficients.

Funding. National Nuclear Security Administration (DE-NA0003856); University of Rochester; New York State Energy Research and Development Authority.

Acknowledgment. This report was prepared as an account of work sponsored by an agency of the U.S. Government. Neither the U.S. Government nor any agency thereof, nor any of their employees, makes any warranty, express or implied, or assumes any legal liability or responsibility for the accuracy, completeness, or usefulness of any information, apparatus, product, or process disclosed, or represents that its use would not infringe privately owned rights. Reference herein to any specific commercial product, process, or service by trade name, trademark, manufacturer, or otherwise does not necessarily constitute or imply its endorsement, recommendation, or favoring by the U.S. Government or any

agency thereof. The views and opinions of authors expressed herein do not necessarily state or reflect those of the U.S. Government or any agency thereof.

Disclosures. The author declares no conflicts of interest.

Data availability. Data underlying the results presented in this paper are not publicly available at this time but may be obtained from the authors upon reasonable request.

References

1. R. Boyd, *Nonlinear Optics*, 4th ed. (Academic Press, New York, 2020).
2. R. A. Haas, "Influence of a constant temperature gradient on the spectral-bandwidth of second-harmonic generation in nonlinear crystals," *Opt. Commun.* **113**(4-6), 523–529 (1995).
3. S. Richard, "Second-harmonic generation in tapered optical fibers," *J. Opt. Soc. Am. B* **27**(8), 1504–1512 (2010).
4. C. R. Phillips and M. M. Fejer, "Efficiency and phase of optical parametric amplification in chirped quasi-phase-matched gratings," *Opt. Lett.* **35**(18), 3093–3095 (2010).
5. K. Regelskis, J. Želudevičius, N. Gavrilin, and G. Račiukaitis, "Efficient second-harmonic generation of a broadband radiation by control of the temperature distribution along a nonlinear crystal," *Opt. Express* **20**(27), 28544 (2012).
6. O. Yaakobi, M. Clerici, L. Caspani, F. Vidal, and R. Morandotti, "Complete pump depletion by autoresonant second harmonic generation in a nonuniform medium," *J. Opt. Soc. Am. B* **30**(6), 1637–1642 (2013).
7. A. Markov, A. Mazhorova, H. Breitenborn, A. Bruhacs, M. Clerici, D. Modotto, O. Jedrkiewicz, P. di Trapani, A. Major, F. Vidal, and R. Morandotti, "Broadband and efficient adiabatic three-wave-mixing in a temperature-controlled bulk crystal," *Opt. Express* **26**(4), 4448–4458 (2018).
8. F. R. Nash, G. D. Boyd, M. Sargent III, and P. M. Bridenbaugh, "Effect of optical inhomogeneities on phase matching in nonlinear crystals," *J. Appl. Phys.* **41**(6), 2564–2576 (1970).
9. R. G. Smith, "Effects of index inhomogeneities on optical second-harmonic generation," *J. Appl. Phys.* **41**(7), 3014–3017 (1970).
10. M. Sabaeian, L. Mousave, and H. Nadgaran, "Investigation of thermally-induced phase mismatching in continuous-wave second harmonic generation: A theoretical model," *Opt. Express* **18**(18), 18732 (2010).
11. J. J. De Yoreo, A. K. Burnham, and P. K. Whitman, "Developing KH₂PO₄ and KD₂PO₄ crystals for the world's most powerful laser," *Int. Mater. Rev.* **47**(3), 113–152 (2002).
12. C. A. Haynam, P. J. Wegner, and J. M. Auerbach, *et al.*, "National Ignition Facility laser performance status," *Appl. Opt.* **46**(16), 3276–3303 (2007).
13. N. Fleurot, C. Cavailler, and J. L. Bourgade, "The Laser Mégajoule (LMJ) project dedicated to inertial confinement fusion: Development and construction status," *Fusion Eng. Des.* **74**(1-4), 147–154 (2005).
14. V. V. Lozhkarev, G. I. Freidman, V. N. Ginzburg, E. V. Katin, E. A. Khazanov, A. V. Kirsanov, G. A. Luchinin, A. N. Mal'shakov, M. A. Martyanov, O. V. Palashov, A. K. Poteomkin, A. M. Sergeev, A. A. Shaykin, and I. V. Yakovlev, "Compact 0.56 petawatt laser system based on optical parametric chirped pulse amplification in KD*P crystals," *Laser Phys. Lett.* **4**(6), 421–427 (2007).
15. O. V. Chekhlov, J. L. Collier, I. N. Ross, P. K. Bates, M. Notley, C. Hernandez-Gomez, W. Shaikh, C. N. Danson, D. Neely, P. Matousek, S. Hancock, and L. Cardoso, "35 J broadband femtosecond optical parametric chirped pulse amplification system," *Opt. Lett.* **31**(24), 3665–3667 (2006).
16. J. Bromage, S.-W. Bahk, M. Bedzyk, I. A. Begishev, S. Bucht, C. Dorrer, C. Feng, C. Jeon, C. Mileham, R. G. Roides, K. Shaughnessy, M. J. Shoup III, M. Spilatro, B. Webb, D. Weiner, and J. D. Zuegel, "MTW-OPAL: A technology development platform for ultra-intense optical parametric chirped-pulsed amplification systems," *High Power Laser Sci. Eng.* **9**, e63 (2021).
17. F. Wang, F. Li, W. Han, W. Wang, P. Li, L. Zhou, Y. Xiang, B. Feng, X. Deng, J. Su, and Q. Zhu, "Large aperture and non-critical phase-matched fourth harmonic generation of Nd:glass lasers," *Matter Radiat. Extremes* **4**(4), 045401 (2019).
18. M. Galletti, P. Oliveira, M. Galimberti, M. Ahmad, G. Archipovaité, N. Booth, E. Dilworth, A. J. Frackiewicz, T. Winstone, I. Musgrave, and C. Hernandez-Gomez, "Ultra-broadband all-OPCPA petawatt facility fully based on LBO," *High Power Laser Sci. Eng.* **8**, e31 (2020).
19. G. Mennerat, J. Rault, O. Bonville, P. Canal, P. Villeval, B. Rainaud, H. Albrecht, D. Lupinski, A. Kokh, N. Kononova, V. Vlezko, K. Kokh, G. Chériaux, M. Pittman, J.-P. Chamaret, and G. Mourou, "115 J, 85% efficiency second harmonic generation in LBO," in *Conference on Lasers and Electro-Optics/Quantum Electronics and Laser Science Conference and Photonic Applications Systems Technologies, OSA Technical Digest (CD)* (Optica Publishing Group, Washington, DC, 2008), Paper CPDA1.
20. A. Kokh, N. Kononova, G. Mennerat, Ph Villeval, S. Durst, D. Lupinski, V. Vlezko, and K. Kokh, "Growth of high quality large size LBO crystals for high energy second harmonic generation," *J. Cryst. Growth* **312**(10), 1774–1778 (2010).
21. H. Kiriyama, N. Inoue, and K. Yamakawa, "High energy second-harmonic generation of Nd:glass laser radiation with large aperture CsLi₆O₁₀ crystals," *Opt. Express* **10**(19), 1028–1032 (2002).
22. X. Chai, F. Wang, B. Feng, X. Feng, L. Zhang, F. Li, W. Han, L. Wang, P. Li, D. Zhu, Y. Jing, and G. Wang, "Deuterium homogeneity investigation of large-size DKDP crystal," *Opt. Mater. Express* **8**(5), 1193–1201 (2018).

23. S. Ji, F. Li, F. Wang, X. Xu, Z. Wang, and X. Sun, "Homogeneity of rapid grown DKDP crystal," *Opt. Mater. Express* **4**(5), 997–1002 (2014).
24. T. Huser, C. W. Hollars, W. J. Siekhaus, J. J. De Yoreo, T. I. Suratwala, and T. A. Land, "Characterization of proton exchange layer profiles in KD_2PO_4 crystals by micro-Raman spectroscopy," *Appl. Spectrosc.* **58**(3), 349–351 (2004).
25. J. Piquard, J. Zaccaro, B. Pintault, C. Maunier, and A. Ibanez, "Origins of optical defects in rapidly grown DKDP crystals," *CrystEngComm* **21**(2), 372–378 (2019).
26. C. Dorrer, I. A. Begishev, S. W. Bahk, and J. Bromage, "High-resolution mapping of phase-matching conditions in second-order nonlinear crystals," *Opt. Mater. Express* **12**(9), 3679–3695 (2022).
27. J. M. Auerbach, P. J. Wegner, S. A. Couture, D. Eimerl, R. L. Hibbard, D. Milam, M. A. Norton, P. K. Whitman, and L. A. Hackel, "Modeling of frequency doubling and tripling with measured crystal spatial refractive-index nonuniformities," *Appl. Opt.* **40**(9), 1404–1411 (2001).
28. W. Han, L. Zhou, F. Wang, F. Li, K. Li, L. Wang, B. Feng, Q. Zhu, J. Su, and G. Mali, "Effect of spatial refractive-index nonuniformities existed in a large-scale rapid growth KDP crystal on third-harmonic conversion," *Optik* **124**(24), 6506–6508 (2013).
29. I. Ya. Itskhoki, M. A. Kashintsev, B. G. Lysoi, and A. A. Solov'ev, "Influence of the longitudinal inhomogeneity of the refractive index of a nonlinear crystal on the parametric gain," *Sov. J. Quantum Electron.* **12**(6), 747–751 (1982).
30. L. P. Mel'nik, N. N. Filonenko, and A. I. Kholodnykh, "Limiting effects of longitudinal optical inhomogeneity of nonlinear crystals on frequency-doubler efficiency," *Sov. J. Quantum Electron.* **9**(1), 13–16 (1979).
31. S. Pelc, C. R. Phillips, D. Chang, C. Langrock, and M. M. Fejer, "Efficiency pedestal in quasi-phase-matching devices with random duty-cycle errors," *Opt. Lett.* **36**(6), 864–866 (2011).
32. C. R. Phillips, J. S. Pelc, and M. M. Fejer, "Parametric processes in quasi-phasematching gratings with random duty cycle errors," *J. Opt. Soc. Am. B* **30**(4), 982–993 (2013).
33. G. Cerullo and S. De Silvestri, "Ultrafast optical parametric amplifiers," *Rev. Sci. Instrum.* **74**(1), 1–18 (2003).
34. C. Dorrer, I. A. Begishev, S.-W. Bahk, and J. Bromage, "Characterization of partially deuterated KDP crystals using two-wavelength phase-matching angles," *Opt. Mater. Express* **11**(3), 774–790 (2021).